Journal of Alloys and Compounds 480 (2009) 351–359

Contents lists available at ScienceDirect

Journal of Alloys and Compounds

journal homepage: www.elsevier.com/locate/jallcom

Microstructure evolution and thermal stability of an Fe-based amorphous alloy powder and thermally sprayed coatings

K. Chokethawai, D.G. McCartney*, P.H. Shipway

Department of Mechanical, Materials and Manufacturing Engineering, Faculty of Engineering, University of Nottingham, University Park, Nottingham NG7 2RD, UK

ARTICLE INFO

Article history:
Received 6 November 2008
Received in revised form 5 February 2009
Accepted 10 February 2009
Available online 23 February 2009

Keywords:
Coating materials
Thermal spraying
Microstructure
Amorphous materials
Thermal analysis

ABSTRACT

High velocity oxy-fuel (HVOF) thermal spraying has been used to produce coatings of an Fe–18.9%Cr–16.1%B–4.0%C–2.8%Si–2.4%Mo–1.9%Mn–1.7%W (in at.%) alloy from a commercially available powder (Nanosteel SHS7170). X-ray diffraction (XRD), differential scanning calorimetry (DSC) and scanning electron microscopy (SEM) were employed to investigate the powder, as-sprayed coatings and annealed coatings which had been heated to temperatures in the range of 550–925 °C for times ranging from 60 to 3900 min. Microhardness changes of the coatings were also measured as a function of annealing time and temperature. The powder was found to comprise amorphous and crystalline particles; the former had a maximum diameter of around 22 μm. The coating was composed of splat like regions, arising from rapid solidification of fully molten powder, and near-spherical regions from partially melted powder which had a largely retained its microstructure. The amorphous fraction of the coating was around 50% compared with 18% for the powder. The enthalpies and activation energies for crystallization of the amorphous phase were determined. Crystallization occurred in a two stage process leading to the formation of α-Fe (bcc), $Fe_{1.1}Cr_{0.9}B_{0.9}$ and $M_{23}C_6$ phases. DSC measurements showed that the first stage occurred at 650 °C. Annealing the coating gave a hardening response which depended on temperature and time. The as-sprayed coating had a hardness of 9.2 GPa and peak hardnesses of 12.5 and 11.8 GPa were obtained at 650 and 750 °C, respectively. With longer annealing times hardness decreased rapidly from the peak.

1. Introduction

In recent years there has been considerable growth in the use of high velocity oxy-fuel (HVOF) thermal spraying for the production of surface coatings to protect components against aggressive operating conditions such as severe wear and/or corrosion [1]. Improvements in the design of HVOF equipment mean that it is now possible to produce coatings which have very low porosity (<1%) from conventional materials such as the wear resistant cermets WC–Co or the corrosion resistant metallic alloy Inconel 625 (Ni–Cr based). Moreover, feedstock powder heating can be controlled such that undesirable reactions in the powder during spraying, e.g. thermal degradation or oxidation, are minimised [2,3]. However, there is a growing industrial demand for new and improved coatings that combine good corrosion resistance with moderate hardness; for example to replace hard chromium plating [4]. Moreover, it is desirable to have the potential to provide protection against aggressive operating environments at elevated temperature.

Certain classes of metallic glass (i.e. amorphous alloys) based around multicomponent Fe–Cr or Ni–Cr alloys have been shown to possess attractive combinations of hardness and corrosion resistance [5,6] and have thus been identified as candidate materials for use as thermally sprayed protective coatings. A number of researchers have investigated the deposition, by thermal spraying, of multicomponent Ni–Cr–B–C- and Fe–Cr–B–C-based alloys which form an amorphous structure when quenched from the melt at high cooling rates, i.e. in the region of 10^7 K s^{-1} [7–9]. Frequently, it has been found that when such alloys are deposited by the HVOF process the final coating contains only a relatively small fraction of the amorphous phase. This can be attributed to several factors, namely: (i) insufficiently high cooling rates of fully melted powder particles when splats are produced during coating deposition; (ii) crystallization of initially amorphous phase material in the coating due to reheating effects as incremental layers are added by rastering the spray gun over the substrate to build up a thick deposit; (iii) the presence in the coating of large unmelted powder particles with a crystalline structure due to incomplete amorphous phase formation in the original starting powder.

Over the last decade there has been consistent progress in exploring multicomponent alloy systems, and synthesizing new alloys, of high glass forming ability (GFA) [10,11]. These are alloys

* Corresponding author. Tel.: +44 115 9513749; fax: +44 115 9513800.
E-mail address: graham.mccartney@nottingham.ac.uk (D.G. McCartney).

0925-8388/$ – see front matter © 2009 Elsevier B.V. All rights reserved.
doi:10.1016/j.jallcom.2009.02.035

which transform to the amorphous state at critical cooling rates at least 10^3 orders of magnitude lower than those needed to produce the earlier types of metallic glass; i.e. involving critical cooling rates in the range of 10^1–10^4 K s^{-1}. Proprietary, Fe based, alloys and powders of high GFA, some of which are apparently suitable for the production of HVOF-sprayed coatings, have thus been developed [12–15]. Because these alloys transform from the liquid to the amorphous state at low critical cooling rates, and also possess relatively high glass transition and crystallization temperatures, the process conditions which exist in HVOF spraying can reportedly be sufficient to produce more than 50% amorphous phase; i.e. significantly greater than could previously be obtained with alloys of low GFA [7–9].

In assessing the suitability for industrial applications of HVOF-sprayed protective coatings which are produced from high GFA alloys, an important issue to be addressed is their thermal stability [16,17]. Thermal stability needs to be considered from two perspectives. First, the possibility of crystallization of the amorphous phase at a relatively low temperature when the coating is in service, which could be deleterious to its properties. Secondly, the opportunity to induce thermally activated phase transformations in a coating by short term annealing treatments above the crystallization temperature (prior to entry into service) which could give enhanced mechanical properties such as hardness.

In the light of these considerations, the main aim of the work reported here was to investigate the microstructural evolution and thermal stability of HVOF-sprayed coatings produced from the commercially available alloy powder SHS7170 (Nanosteel Company Inc., Providence, Rhode Island, USA). This alloy is based around an Fe–Cr–B composition which is reportedly a high GFA alloy [12,15]. Whilst there is a specific emphasis in the paper on the behaviour of HVOF-sprayed coatings, we also report the results of a parallel study conducted on the gas-atomised feedstock powder used in the spraying experiments as this material provides valuable base-line information. The techniques of X-ray diffraction (XRD), scanning electron microscopy (SEM), microhardness testing and differential scanning calorimetry (DSC) were all employed to characterize powders and coatings before and after short and longer term heat treatments in the temperature range of 500–925 °C.

2. Experimental

2.1. Materials and HVOF thermal spraying

A commercial Fe–Cr–B based, gas-atomised powder (SHS7170) with a nominal size range of −53 to +15 μm was obtained from the Nanosteel Company Inc., Providence Rhode Island, USA. The nominal alloy composition, as given by the manufacturer's data sheet, was 18–22%Cr, 3.9–7%Mo, 5–6.5%W, 2–4.9%Mn, 0.3–1.9%Si, 3–4.1%B, and <0.4%C (all in wt.%) with the balance being Fe. The chemical composition measured by an external accredited laboratory using X-ray fluorescence (XRF) spectrometry, inductively coupled plasma (ICP) spectrometry and Leco combustion analysis gave the following alloy composition (in at.%): Fe–18.9%Cr–16.1%B–4.0%C–2.8%Si–2.4%Mo–1.9%Mn–1.7%W (hence its description as an Fe–Cr–B-based alloy). Prior to spraying, the powder was sieved to obtain a nominal size range of −45 to +15 μm with a d_{50} value of 31 μm in order to optimise the coating characteristics. Thermal spraying was undertaken using a Metallisation Met Jet II high velocity oxy-fuel system. This HVOF system is described in detail elsewhere [18]. Briefly, the fuel is liquid kerosene which is combusted with pure oxygen at a pressure of around 8 bar in the combustion chamber of the gun. The combustion products flow through a converging-diverging nozzle and powder is injected, downstream of the throat, through two radial ports into the hot, high-speed gas. The powder is then accelerated and heated by the gas stream as it flows along a parallel-sided barrel; in the present work a barrel of length 100 mm was employed. Spray parameters were optimised to minimise both the deposit porosity and degree of oxidation of the particles during spraying. Table 1 lists the spray parameters employed in this study. Coatings were deposited onto flat, grit-blasted and degreased mild steel substrates approximately 25 mm × 60 mm × 2 mm in size and by scanning the gun across the substrate in a number of passes a coating was built up. A gun-substrate stand-off distance of 355 mm was used and the gun traverse speed across the substrate was ∼1 ms^{-1}. Typically, 40 passes of the gun were employed to achieve coatings approximately 320 μm thick. During deposition the average substrate temperature was maintained below 220 °C using compressed air jets.

Table 1
Parameters used in the deposition of the SHS7170 powder using the Met Jet II gun.

Parameter	Value
Kerosene flow rate	0.39 l min^{-1}
Oxygen flow rate	895 l min^{-1}
Powder carrier gas flow rate	7.5 l min^{-1}
Powder feed rate	80 g min^{-1}
Stand-off distance	355 mm

2.2. Heat treatment of powder and coatings

The heat treatment of the powder and coating samples was carried out in a tube furnace under an argon gas atmosphere to prevent oxidation. Samples were heated from room temperature to the heat treatment temperature at a heating rate 20 K/min and were then held for the appropriate time before being furnace cooled back to room temperature. One set of heat treatments was performed for a fixed time of 60 min at the following temperatures: 550, 650, 750 and 925 °C. A second set of heat treatments was performed at only two temperatures, namely 650 and 750 °C, with holding times of 60–3900 min at 650 °C and 20–120 min at 750 °C.

2.3. Materials characterisation

Microstructural examination of powder particles and coatings was performed using a FEI XL30 scanning electron microscope using both secondary electron (SE) and back scattered electron (BSE) imaging. Selected samples were examined in a SEM with a field emission gun to achieve better resolution of fine scale microstructural features. For microstructural examination, powder particles and coatings were mounted in conducting resin, ground and diamond polished to a 1 μm finish. In the case of coatings, sections were taken perpendicular to the coating–substrate interface for examination. In some cases coating samples were etched in a solution comprising one part HCl, one part HNO_3 and one part H_2O for 4–10 s. In order to measure coating porosity, image analysis was performed on SEM/BSE images obtained from polished cross-sections. Ten images were recorded at a magnification of 2500× and Scandium software was employed to calculate the mean pore volume fraction mean pore size. Semi-quantitative energy dispersive X-ray analysis (EDXA) was also utilised to aid phase identification through chemical microanalysis of elements with atomic number >6. Powders and coatings were also investigated by X-ray diffraction using a Siemens D500 diffractometer employing monochromatic Cu Kα ($\lambda = 0.15406$ nm) radiation. XRD analysis of the coatings was performed on the top surface. XRD scans were performed with a 2θ step size of 0.05° and a dwell time per step of 2 s in the 2θ range of 30–90°. The microhardness of the as-sprayed and heat treated coatings was measured using a LECO M-400 microhardness tester with a load of 2 N (200 gf) and a dwell time of 15 s. The hardness of these samples was measured along the mid-plane of coating cross-sections, parallel to the coating–substrate interface. The mean value of 10 measurements is quoted as the hardness of the specimen and the error is given as the standard error in the mean, i.e. $\sigma/\sqrt{n}$ where σ is one standard deviation and n is the number of measurements made.

2.4. Differential scanning calorimetry

The DSC measurements were performed using a differential-temperature type DSC (TA Instruments model SDT Q600) using recrystallized alumina sample pans. Coating samples for DSC were obtained by carefully removing small areas of coating from the substrate to obtain specimens approximately 4 mm in diameter by approximately 0.45 mm thick, with a sample weight of typically 60 mg. DSC powder samples were obtained by filling the alumina sample pan with approximately 60 mg of loose powder. All runs were performed under a purified argon gas atmosphere (flow rate ∼100 ml min^{-1}). The temperature scale was calibrated using the melting point (onset) of pure aluminium (660 °C) and gold (1064 °C). DSC scans were carried out at heating rates of 10, 20, 30, 40 and 50 K/min in the temperature range of 20–1000 °C and all traces were corrected by subtracting the instrumental baseline (obtained from a DSC run with two empty pans). From these corrected traces, characteristic temperatures for various phase transformations were determined and apparent activation energies of reactions were estimated, using the Kissinger method [19], based on the peak shifts observed in the linear heating rate DSC curves at the different heating rates employed.

3. Results

3.1. Powder characteristics

Fig. 1 shows the XRD pattern of the gas-atomised SHS7170 Fe–Cr–B-based powder which shows one series of peaks that corre-

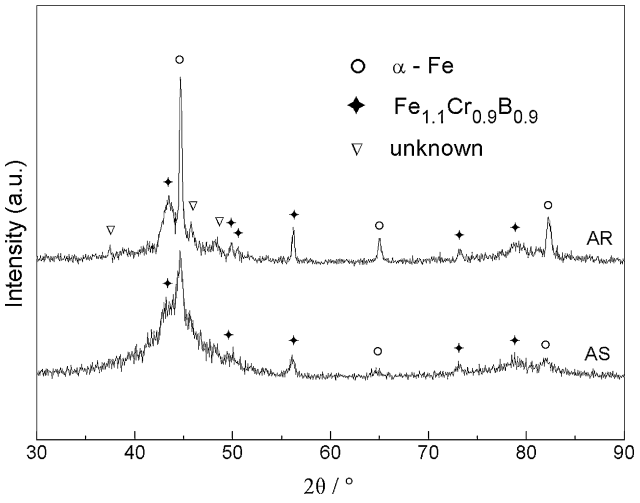

Fig. 1. XRD patterns in the range $2\theta = 30–90^\circ$ for as-received gas-atomised powder (AR) and as-deposited HVOF-sprayed coating (AS) indexed as α-Fe and $Fe_{1.1}Cr_{0.9}B_{0.9}$. There are three minor peaks from the powder which could not be identified.

sponds to a body centred cubic (bcc) phase with a lattice parameter ~0.2880 nm, i.e. close to that of α-Fe ($a_0 = 0.2902$ nm) and a second set of peaks that corresponds to the boride phase $Fe_{1.1}Cr_{0.9}B_{0.9}$ (JCPDS file #072-1073). There is also a distinct diffuse diffraction halo centred around $2\theta \sim 44^\circ$ which suggests the possibility of either amorphous phase or material with a nanocrystalline grain structure. Fig. 2 shows BSE images of powder particle cross-sections and it is clear that the smaller particle, Fig. 2(a), (~18 μm in diameter) has a featureless appearance and was presumably amorphous whereas the larger particle, Fig. 2(b), (~45 μm in diameter) shows a two-phase structure with a large volume fraction of a dark-contrast, needle-like or acicular phase in a lighter contrast matrix. The largest particle diameter on a polished cross-section that exhibited a featureless, i.e. amorphous, structure was approximately 22 μm. The higher magnification image of a large particle, Fig. 2(c) reveals that the needle-like phase is clearly of lower mean atomic number (darker contrast) and EDXA showed that it contained significant amounts of both Fe and Cr. The lighter regions contained a lower proportion of Cr as well as being enriched in Mo, W, Mn and Si. It is concluded therefore that the dark contrast needles and lighter contrast matrix correspond respectively to the $Fe_{1.1}Cr_{0.9}B_{0.9}$ boride phase and the bcc α-Fe phase identified from XRD analysis and the crystalline peaks are from the phases in the larger powder particles.

The DSC traces of the alloy powder obtained at different heating rates are shown in Fig. 3. At all heating rates two exothermic peaks were obtained. When a sample was cooled back down to room temperature in the DSC and the heating run repeated the exothermic peaks disappeared. This behaviour suggests that the first peak was due to primary crystallization and on further heating, the second peak arose from a residual amorphous phase crystallising in a second step into boride and/or carbide phases in an α-Fe matrix [20]. It was not possible to identify a glass transition temperature from the DSC traces; probably because the weight fraction of fully amorphous powder in the sample was not sufficiently large. However, the peak temperatures for the first and second peaks could be accurately determined and these data are provided in Table 2 for the different heating rates employed. The enthalpy of crystallization of the powder sample (which is a mixture of amorphous and crystalline particles) was calculated to be $20 \pm 2\,J\,g^{-1}$ for the first peak and $25 \pm 4\,J\,g^{-1}$ for the higher temperature peak. Activation energies, E_a, for the two reactions were determined by the Kissinger method [19] and were determined to be 375 ± 10 and $333 \pm 18\,kJ\,mol^{-1}$ for the first and second peaks, respectively.

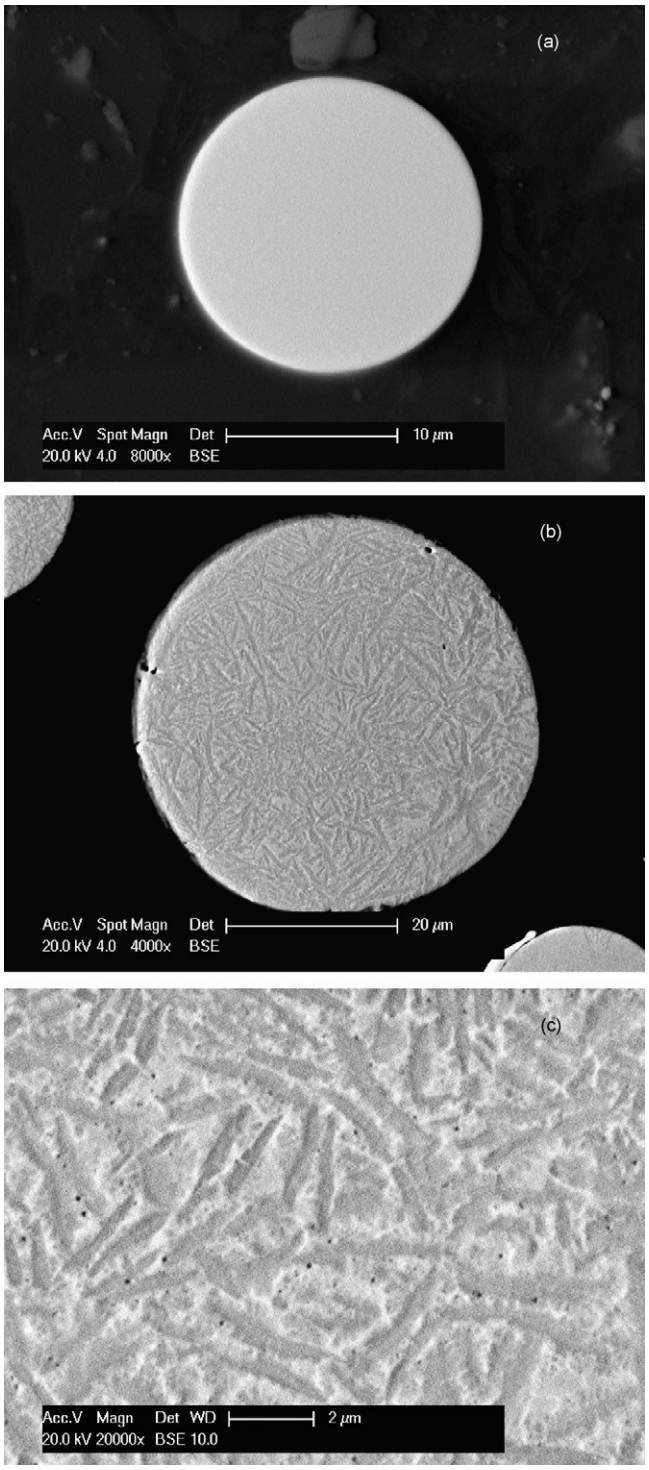

Fig. 2. BSE images of cross-sections through gas-atomised powder particles showing the difference in structure between small (a) and large (b) diameter particles. (a) Appears largely featureless whereas (b) reveals the presence of two distinct phases. (c) Higher magnification view of the particle shown in (b) revealing dark contrast needles and lighter contrast matrix.

To further investigate the thermal stability of the alloy powder, samples were annealed for 60 min at 550, 650, 750 and 925 °C. Fig. 4 shows the XRD patterns obtained from these experiments along with the pattern from the as-received powder. It is clear from the continued presence of the diffraction halo around $2\theta \sim 44^\circ$ that the amorphous phase was thermally stable up to approximately 650 °C. Also, the peaks from the phases α-Fe and $Fe_{1.1}Cr_{0.9}B_{0.9}$,

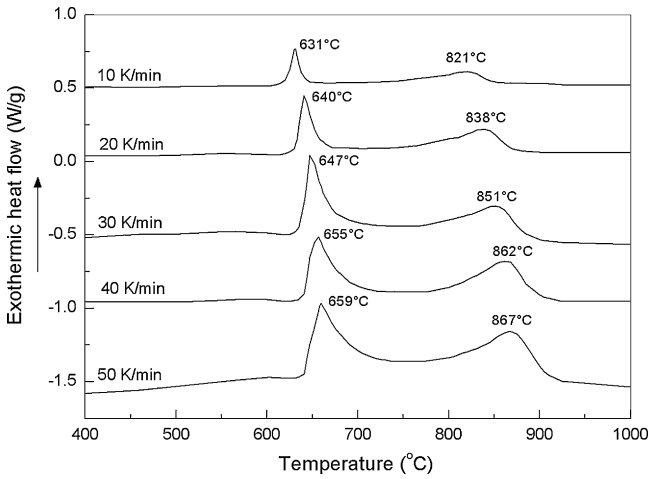

Fig. 3. DSC traces obtained from the as-received SHS7170 powder at heating rates 10, 20, 30, 40 and 50 K/min.

Table 2
DSC peak temperatures obtained from SHS7170 powder and HVOF-sprayed coatings at different heating rates.

Heating rate (K/min)	Sample type	Temperature of 1st peak (°C)	Temperature of 2nd peak (°C)
10	Powder	631	821
	Coating	632	760
20	Powder	640	838
	Coating	640	778
30	Powder	647	851
	Coating	646	790
40	Powder	655	862
	Coating	653	799
50	Powder	659	867
	Coating	660	810

present in the XRD pattern of the as-received sample, show no detectable change with annealing temperature up to 650 °C. Since crystallization occurred around 640 °C according to DSC analysis, it can be concluded that it involved primary crystallization of α-Fe or $Fe_{1.1}Cr_{0.9}B_{0.9}$ since no additional phases were detected on the 650 °C XRD pattern. On annealing at 750 and 925 °C a new crystalline phase formed which was identified as $M_{23}C_6$ carbide (M = Cr, Fe, W, Mo) (JCPDS file # 005-0721) and the quantity of this phase clearly increased with annealing temperature as evidenced by the increasing XRD peak intensities for $M_{23}C_6$. It would seem, therefore, that the second peak on the DSC traces shown in Fig. 3 is associated with carbide phase precipitation.

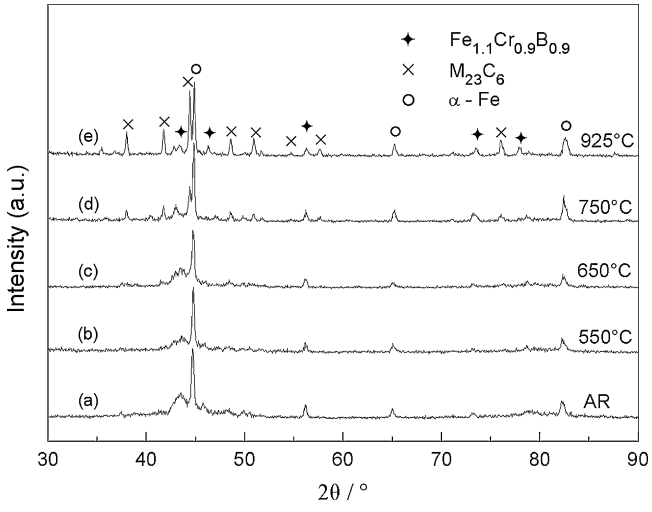

Fig. 4. XRD patterns in the range $2\theta = 30–90°$ for as-received, gas-atomised powder (AR) and powder heat-treated for 60 min at the temperatures indicated on the plots.

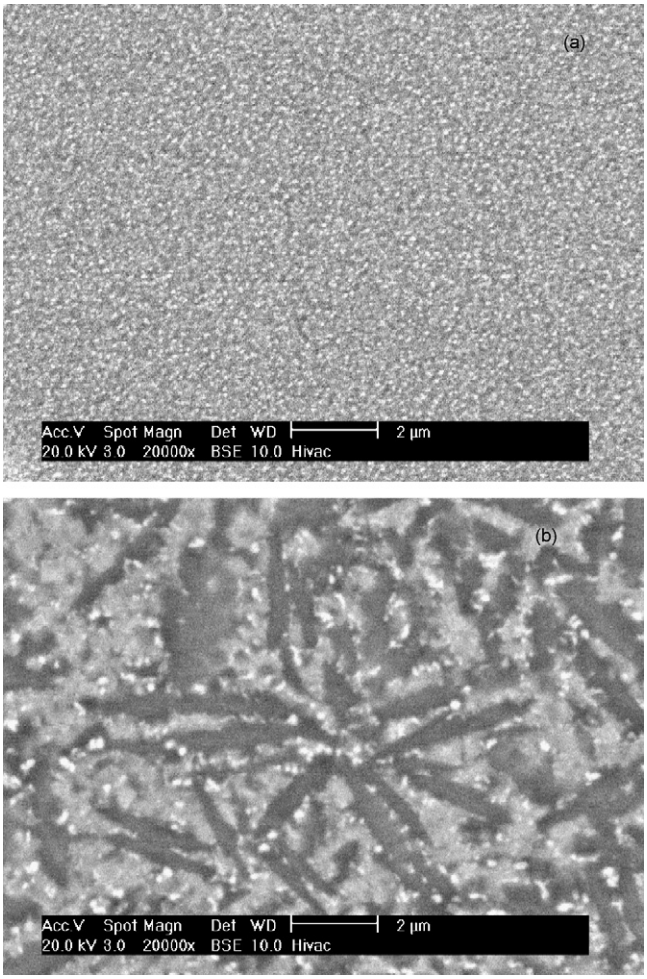

Fig. 5. BSE images of cross-sections through gas-atomised powder particles showing the difference in structure between small (a) and large (b) diameter particles following heat treatment at 750 °C for 60 min. In (b) the boride phase is dark, the Fe-matrix grey and the carbide phase bright.

Fig. 5(a) and (b) shows BSE images of the cross-sections of small and large powder particles, respectively following heat treatments at 750 °C. It is seen that sub-micron precipitation is observable in the small diameter powder, in contrast with the featureless appearance of Fig. 2(a). In Fig. 5(b) there is also seen to be fine scale precipitation of carbide phase particles (bright contrast) between the larger boride needles (dark contrast) and the grey contrast α-Fe matrix. This image should be compared with the non-heat treated powder of similar diameter, Fig. 2(c) which shows only boride needles in an α-Fe matrix. Following heat treatment at 925 °C, similar precipitation was observed but found to be coarser whereas a 550 °C heat treated sample exhibited the same microstructural features as the powder before heat treatment when examined in the SEM.

3.2. Characteristics of the coatings

The XRD pattern from the as-sprayed top surface of a coating (AS) is shown in Fig. 1 along with that from the powder (AR). As before the peaks can be identified as belonging to α-Fe and $Fe_{1.1}Cr_{0.9}B_{0.9}$. One notable difference between the AS and AR traces

is that the peaks of the α-Fe phase from the coating appear broader and of lower relative intensity. Also the halo in the XRD pattern from the coating (AS) around $2\theta \sim 44^\circ$ is somewhat broader. These features could suggest either that there was a greater proportion of the amorphous phase in the coating or that more of the α-Fe had a sub-100 nm grain size; both create the type of peak broadening observed. No peaks from oxides such as chromium or iron oxides could be detected.

The sprayed coating appears to have low overall porosity as seen from the SEM image, Fig. 6(a). The porosity was found to be approximately 0.2 vol% from the image analysis measurements with a mean pore size of 0.8 μm. At higher magnification, following etching, various different microstructural features can be observed, Fig. 6(b). Unmelted or partially melted crystalline particles retained from the original powder etch strongly and appear as either near-spherical or deformed and elongated particles in the coating (labelled P) whereas the featureless regions (labelled F) are believed to arise from fully melted powder particles which formed lenticular splats on impact and then solidified [1,2,18]. The original, needle-like boride phase is readily discerned in the regions labelled P whereas the low etching response of the splat regions (F) could suggest an amorphous structure. Fig. 6(c) shows a BSE image of an unetched sample at increasing magnification; specifically a boundary between a partially melted, near-spherical crystalline particle (P) and a splat like region (F). The different levels of contrast seem to indicate featureless or finer scale features in the splat regions compared with the retained powder particles. Also visible are very dark lines at boundaries between splats and retained powder particles. EDXA showed that the very dark lines were rich in chromium and also contained oxygen suggesting that they are an oxide phase probably produced by oxidation during spraying. However, there was clearly insufficient oxide phase to be detected by XRD.

The DSC traces of coating samples obtained at different heating rates are shown in Fig. 7 and the peak temperatures for the first and second peaks at the different heating rates are given in Table 2. In the coating, the first peak occurred at similar temperatures to that found for the powder and is ascribed to primary crystallization. However, the traces show that this first peak had, at all heating rates, a well defined shoulder to the low temperature side of the peak with an onset consistently around 60 K below the actual peak. The enthalpy of the total reaction (shoulder plus main peak) was found to be $55 \pm 5\,\mathrm{J\,g^{-1}}$. As in the case of powder samples, a higher temperature peak was also observed with an enthalpy estimated to be $16 \pm 5\,\mathrm{J\,g^{-1}}$ which would appear to represent a second stage of crystallization. Activation energies, E_a, for the two reactions in the coating samples were again determined by the Kissinger method [19] and were found to be 385 ± 12 and $290 \pm 20\,\mathrm{kJ\,mol^{-1}}$ for the first and second peaks, respectively.

To investigate their thermal stability, coating samples were annealed in an identical manner to the powder, i.e. for 60 min at 550, 650, 750 and 925 °C. Fig. 8 shows the XRD patterns obtained along with the patterns for the as-received powder (AR) and as-sprayed coating (AS). Broadly, the phase changes observed are similar those seen in the powder samples following heat treatment. However, some small differences in behaviour at 650 °C can be seen concerning the changes to the amorphous halo around $2\theta \sim 44^\circ$. Following 650 °C heat treatment, a more pronounced boride phase peak at around 43° had begun to appear in coating samples, whereas this is less visible in the 650 °C XRD pattern of the powder sample (Fig. 4). A difference can also be seen in the carbide phase peaks which appear broader in the coating samples following heat treatment at 750 and 925 °C; suggesting a more disordered crystal structure.

Fig. 9(a)–(c) shows high magnification BSE images of cross-sections of coatings following heat treatment at 550, 750 and 925 °C, respectively. Specifically they show the microstructural changes of the retained powder particles, P, and splat-like regions

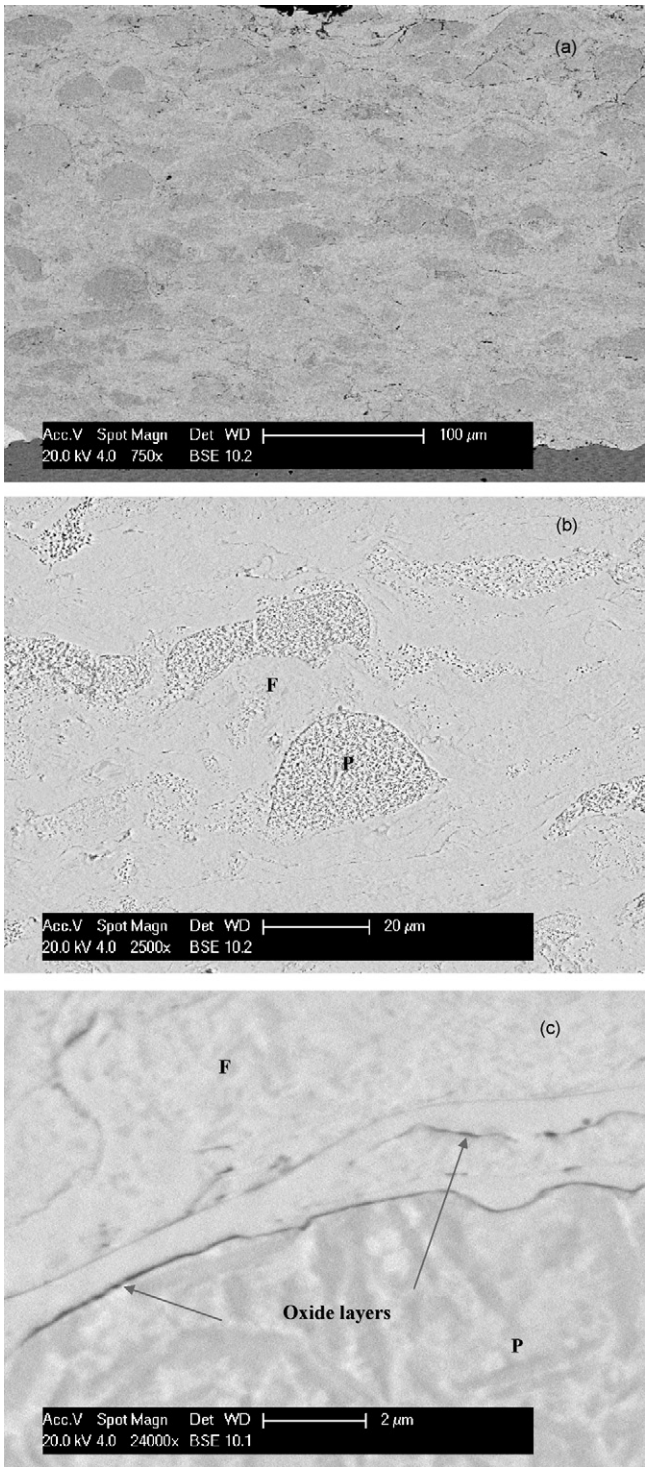

Fig. 6. BSE images of cross-sections through the as-sprayed coating. (a) Low magnification image showing coating with little porosity. (b) Microstructure following etching showing regions corresponding to: powder particles that have not fully melted (P); and solidified splats (F). (c) Unetched and shows regions P and F at higher magnifications. Thin dark bands are oxide layers.

(melted and re-solidified powder), F. In Fig. 9(a), taken from the sample heat treated at 550 °C, the retained powder structure of dark contrast boride and light contrast α-Fe matrix is visible in region P. In region F, a light contrast matrix is visible and there is a region between P and F where borides are visible but there is a lower fraction compared with region P. In Fig. 9(b), from the sample annealed at 750 °C, sub-micron bright contrast precipitates are visible along

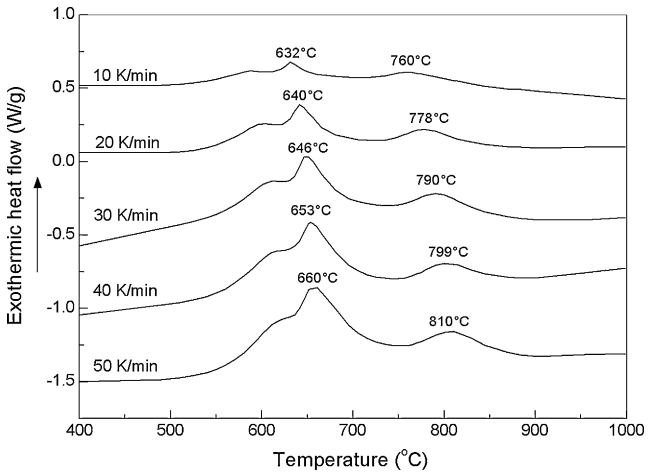

Fig. 7. DSC traces obtained from the as-sprayed coating at heating rates 10, 20, 30, 40 and 50 K/min.

with dark, micron sized needles and a grey matrix. The precipitates were too small for EDXA to be carried out but it seems reasonable to presume (from the previous EDXA of coarser particles) that the bright precipitates are carbides and the dark needles are borides. At the same heat treatment temperature the region P shows dark, light and grey contrast features of micron-sized proportions which are likely to be boride, carbide and Fe-matrix, respectively. At the highest heat treatment temperature of 925 °C the region P and F both show micron sized phase regions with three different contrast levels clearly visible which would correspond to the three phases identified from the XRD pattern, Fig. 8.

3.3. Coating microhardness

The as-sprayed coating had a microhardness of 9.2 ± 0.1 GPa and following annealing for 60 min at 550, 650, 750 and 925 °C the microhardness was found to change as shown by the data in Table 3. It increased for temperatures up to 750 °C but at 925 °C had a value similar to that of the as-sprayed coating. These changes suggest that devitrification significantly increases the hardness compared with the as-sprayed structure but that as phase coarsening and solute diffusion become more extensive the hardness begins to diminish significantly. To investigate more fully the combined effects of time

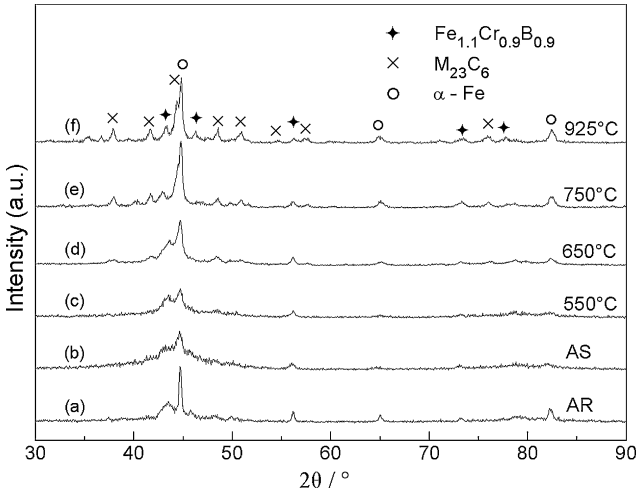

Fig. 8. XRD patterns in the range 2θ = 30–90° for as-received, gas-atomised powder (AR), as-sprayed coating (AS) and coating samples heat-treated for 60 min at the temperatures indicated on the patterns.

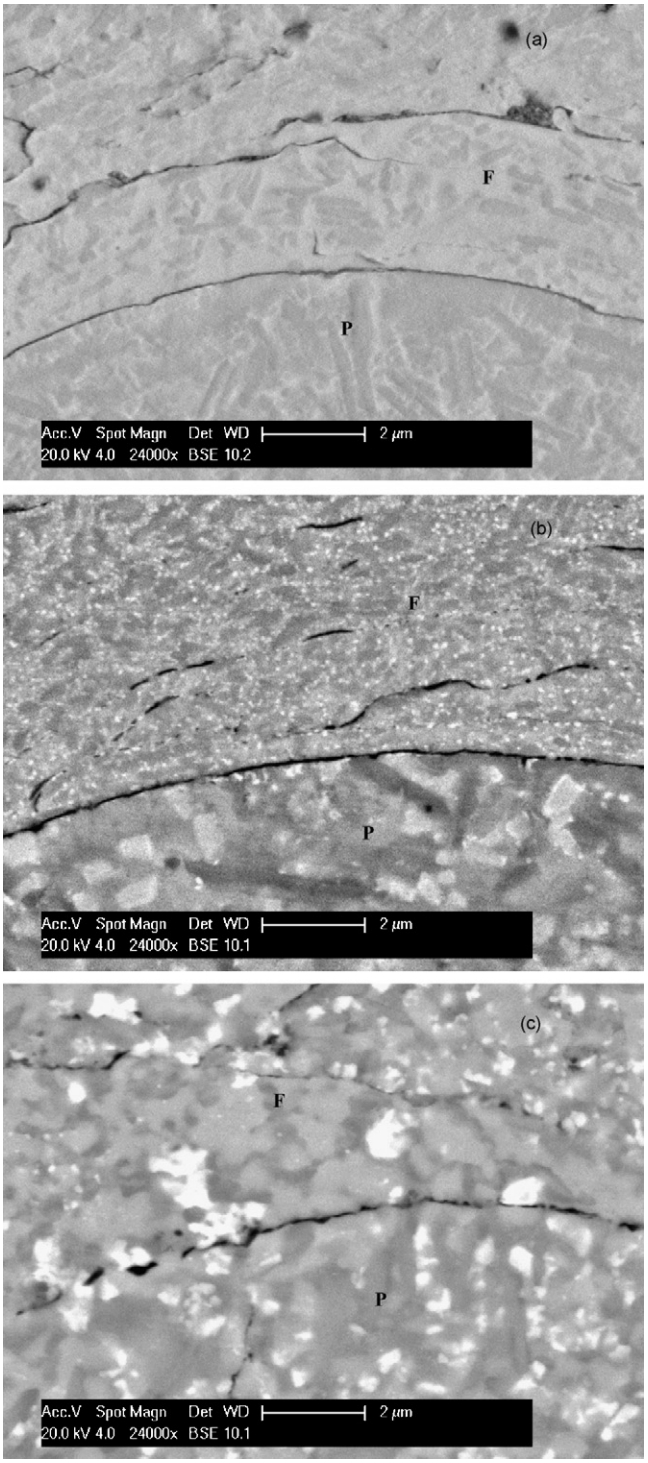

Fig. 9. BSE images of coatings following heat treatment, showing regions corresponding to powder not fully melted (P) and solidified splats (F). (a–c) Correspond to annealing for 60 min at 550, 750 and 925 °C, respectively.

Table 3
Microhardness of the coating following heat treatment for 60 min at various temperatures.

Heat treatment temperature (°C)	550	650	750	925
Mean microhardness (GPa)	9.1	10.9	11.7	9.2
Standard error (GPa)	0.1	0.2	0.1	0.2

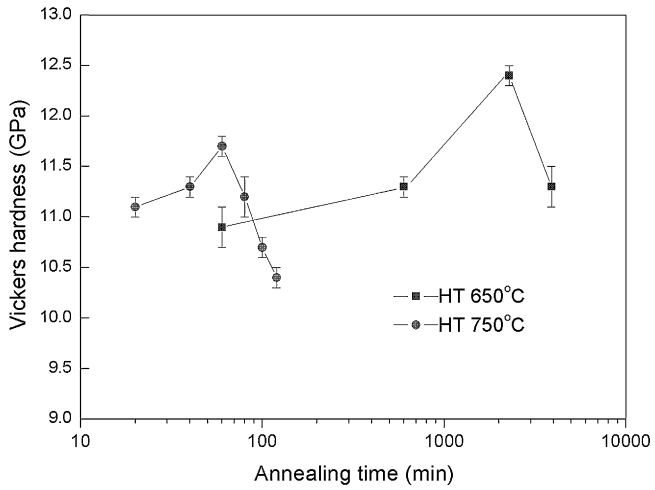

Fig. 10. Plots of Vickers microhardness versus annealing time (log scale) for coatings annealed at 650 and 750 °C showing that the maximum in hardness varies with heat treatment temperature (microhardness of as-sprayed coating = 9.2 ± 0.1 GPa).

and temperature on microhardness, samples were annealed for various times at two temperatures, namely 650 and 750 °C. These were chosen to be just above the first DSC crystallization peak and just below the second DSC peak, Fig. 7. The results obtained are shown by the graphs plotted in Fig. 10. At both temperatures, hardness increased at first and then decreased. At 750 °C the peak hardness is seen to occur after around 60 min with a value of 11.7 GPa whereas at 650 °C the peak was not reached until approximately 2000 min and had a value of 12.4 GPa. Clearly, increasing the temperature reduced the time to reach the peak hardness but the maximum hardness that could be achieved decreased with increasing annealing temperature. Therefore it would appear that a high hardness relies on achieving a nanoscale precipitate distribution.

4. Discussion

The main questions addressed in the present study concerned microstructure evolution and the effect of exposure to elevated temperature on microstructure and microhardness of HVOF-sprayed coatings using the multicomponent Fe–Cr–B-based alloy powder (SHS7170). This alloy has previously been reported to be one of high GFA [15]. The main finding of the present work is that coatings sprayed with a liquid fuel HVOF gun are only partially amorphous. On heating in a DSC, crystallization of the amorphous phase begins at around 640 °C. Thus below 640 °C coatings are thermally stable but above it crystallization leads to significant changes in microstructure and microhardness. The extent of the changes depend on both temperature and time. In the sections which follow, the development of the coating microstructure will be considered and its response to elevated temperature exposure will be analysed; comparisons between the behaviour of powder and coatings will also be made. Furthermore, the DSC results will be considered and the activation and transformation energies assessed.

4.1. As-sprayed coating microstructure

The partially amorphous, partially crystalline nature of the coatings is clear from the following: (i) the XRD pattern of Fig. 1; (ii) the SEM images of Fig. 6; (iii) the DSC traces of Fig. 7. As has been discussed previously [18], coatings deposited by the liquid fuel gun employed here show clear evidence of the impact of partially melted powder particles (generally those of large diameter) which have near-spherical or deformed spherical shapes in the coating and fully melted powder (generally of smaller diameter) which flatten and solidify to give characteristic lenticular splat features in the coating. As seen in Fig. 2(b), the larger particles in the original powder possess a two-phase structure of $Fe_{.1}Cr_{0.9}B_{0.9}$ plates in a matrix of α-Fe and this microstructure is retained in the as-sprayed coating, see Fig. 6. Smaller powder particles are apparently heated to a significantly higher temperature in the gas jet, as predicted by numerical modelling studies [21], become fully melted and, on impact, form lenticular splats which solidify rapidly. The cooling rate of such splats is estimated to be of the order of 10^7 K s^{-1} [22] and in this high GFA alloy they are thus expected to form an amorphous structure.

A consideration of the structures formed in the original powder particles supports this analysis. It is seen from Figs. 1, 2(a) and 3 that a significant fraction was amorphous and it was observed that the maximum diameter of a fully amorphous particle was ~22 μm. Using the well known relationship between powder diameter and cooling rate [23], 22 μm particles of an Fe-based alloy are estimated to cool at around 10^3–10^4 K s^{-1} during their manufacture by gas atomisation. Thus this cooling rate range can be seen to be an estimate for the critical cooling rate for glass formation in the alloy. This is well below the cooling rate of splats and so confirms that splats are likely to be amorphous.

The present observations on HVOF coating formation are consistent with work reported by Branagan et al. [15] on the same alloy but deposited by wire-arc spraying. Branagan et al. [12] also observed similar mixed amorphous/crystalline structures in HVOF and air plasma sprayed coatings using a high GFA alloy of nominal composition $Fe_{63}Cr_8Mo_2Si_1Al_4B_{17}C_5$. In comparison, the present alloy's composition was $Fe_{52}Cr_{19}Si_3Mo_2W_2Mn_2B_{16}C_4$, i.e. of similar B and C levels but richer in Cr (at the expense of Fe) and with W and Mn replacing Al and Si.

4.2. Analysis of DSC data

The DSC traces indicate that the amorphous fraction of the coating crystallises in two stages, a main peak at around 645 °C and a smaller secondary peak at ~790 °C, depending on the heating rate (see Fig. 7 and Table 2). A comparison with the DSC thermograms for the powder shows similar temperatures for the first crystallization peak but in the powder the 2nd peak seems to appear at a significantly higher temperature (around 850 °C). Furthermore, in the coating the first peak exhibits a distinct shoulder whereas this is absent in the powder traces, compare Figs. 3 and 7 for powder and coating, respectively. Overall, the decomposition pathway appears to follow that suggested by Lu [20], i.e. in the first step the amorphous phase crystallises into a primary phase and a residual amorphous phase of different composition. At a higher temperature this residual phase crystallises in a second step into one or more crystalline phases. Such a two stage crystallization process is common in Fe-based amorphous alloys and often leads to nanoscale crystallization products [11,20,24–26]. The reason for the formation of a pronounced shoulder on the low temperature side of the first DSC peak obtained from coating samples needs to be examined. Such a shoulder was not present on the DSC traces from powder, see Figs. 3 and 7. The shoulder on the low temperature side is possibly the manifestation of the early crystallization of amorphous material in the coating that was significantly reheated for a short period during successive passes of the spray gun whilst depositing multiple layers. Local reheating would allow the formation of pre-existing crystalline nuclei or relaxation of the amorphous state, as proposed by Graydon et al. [27], which leads to a portion of the amorphous phase crystallizing at lower temperature. Local reheating during spraying and amorphous phase relaxation could also be the reason for the lower temperature of the second DSC peak in coating samples.

Activation energy is regarded as an important parameter characterizing the crystallization process and for the first peak it was determined to be 375 kJ mol^{-1} for the powder and 385 kJ mol^{-1} for the coating using the Kissinger method [19]. The errors associated with the measurements mean that these values should be regarded as essentially the same. For the second peak, the activation energy is lower than for the first peak and is also found to differ somewhat for powder and coating, the values being 333 and 290 kJ mol^{-1}, respectively. This difference could also be due to reheating of the coating during spray deposition. Broadly, these activation energies are in line with values obtained in other multicomponent Fe-based amorphous alloy systems, for example Chen et al. [26].

Considering now the enthalpies associated with the two crystallization stages, the value obtained for the first stage is 20 J g^{-1} for the powder and 55 J g^{-1} for the coating. For the second stage the respective values for powder and coating are 25 and 16 J g^{-1}, respectively. The much larger value for the coating indicates that a much larger portion of amorphous phase formed as a result of spraying the powder. This is consistent with the more pronounced amorphous halo around $2\theta = 42–48^\circ$ of the XRD pattern from the coating, Fig. 1. The powder was clearly a mixture of amorphous and crystalline particulate and the largest particle diameter that was amorphous (as assessed by the absence of contrast in the SEM) was ~22 μm. In a separate experiment, the powder particle size distribution was measured using a laser diffractometer-based method and from the resultant size distribution it was found that 18 vol% was below 22 μm in size. This is equivalent to 18 wt.% as all powder particles are assumed to have the same density. Therefore the measured value of 20 J g^{-1} for the enthalpy of the first crystallization peak of the powder corresponds to a value of approximately 110 J g^{-1} (i.e. 5.6 kJ mol^{-1}) for the material, taking account of the fact that only 18 wt.% of the powder was actually in the amorphous state. This is similar to the value of 127 J g^{-1} reported by Branagan et al. [12,16] for related Fe-based amorphous alloys.

As the first crystallization enthalpy of the coating was 55 J g^{-1} this would suggest that the amorphous fraction in the coating was around 50%. This increase in amorphous fraction occurs because in the thermal spray gun a significant proportion of the powder is melted and these molten particles give rise to solidified lenticular splats in the coating, as seen in the SEM images of Fig. 6(a) and (b). Splats cool at a sufficiently high rate (around 10^7 K s^{-1} [22]) to have an amorphous structure and the 50% amorphous fraction measured by DSC arises from these rapidly quenched splats. The unmelted powder particles seen in the coating retain their crystalline structure during spraying. In contrast to this, Branagan et al. [15] reported that when a coating of the same alloy was produced by wire-arc spraying (with a cored wire) the amorphous fraction was 70%. This is greater than the present HVOF coatings because wire-arc spraying involves converting all the solid feedstock into fully molten droplets which are then expected to become amorphous when they strike the substrate, cool rapidly and solidify; suggesting a 100% amorphous coating could be achieved. The reason that it was only 70% amorphous is probably due to re-heating of the coating during deposition of successive layers leading to recrystallization of the original amorphous phase.

4.3. Microstructural and microhardness changes during heat treatment

Heat treatment temperatures were selected to be: (i) below the first crystallization peak at 550 °C; in between the first and second peaks at 650 and 750 °C; (iii) well above the second crystallization peak at 925 °C. It is evident from Figs. 4, 5, 8 and 9 that phase changes and microstructural evolution proceed in a similar manner in powders and coatings. Annealing for 60 min at 550 and 650 °C produced no new phases that could be detected in the XRD diffractorgrams. The main difference between these two heat annealing temperatures was the appearance of more pronounced boride and α-Fe peaks particularly in the coating. Therefore this suggests that the primary crystallization stage at ~640 °C involves decomposition of the amorphous phase into these two phases with a residual amorphous phase which decomposes at a higher temperature. Annealing at 750 °C for 60 min led to the first appearance of the $M_{23}C_6$ phase in both powder and coating samples. The $M_{23}C_6$ peaks became much stronger and sharper following annealing at 925 °C. This suggests that the main change in the second stage of crystallization was the precipitation of the carbide phase and α-Fe and that most of the boride phase was produced in the first crystallization reaction.

The main microstructural change as a result of annealing was the formation of a nanoscale mixture of crystalline phases, i.e. a nanoscale composite, from fully amorphous regions. This is seen most clearly in Fig. 5(a) showing a fine powder particle annealed at 750 °C and in Fig. 9(b) (region F) showing a splat region of a coating. In coarser powder particles, nanoscale precipitates also formed following annealing at 750 °C in between the boride plates. The main effect of annealing a coating at 925 °C was to produce a significantly coarser precipitate distribution as seen in Fig. 9(c) where both F and P regions of a coating display micron sized precipitate features as opposed to the nanoscale features seen following annealing at 750 °C. Following annealing at 925 °C, similar precipitate distributions were found in fine and coarse gas-atomised powder particles.

The coatings exhibit a hardening response which depends on heat treatment time and temperature. The hardness in the as-sprayed coating is 9.2 GPa and this is increased to a maximum of 11.8 GPa after heat treatment at 750 °C and a maximum of 12.5 GPa after heat treatment at the lower temperature of 650 °C. It is clear that devitrification of the amorphous phase is the main reason for the increase in hardness seen initially. This devitrification will lead to nanoscale α-Fe grains and nanoscale boride/carbide precipitates. It has also been suggested [28] that compositional changes to the residual amorphous phase can also have an important hardening effect. The higher peak hardness occurs at a lower annealing temperature even though carbide/boride precipitation is more pronounced at the higher temperature. Therefore, it is evident that the relationships between microstructural changes and microhardness are complex and that further work is needed to clarify this behaviour. With longer annealing times, the hardness begins to decrease at both the annealing temperatures. It is observed that grain and precipitate coarsening occurs with increased holding time and it is likely that solid solution strengthening of the α-Fe phase through solute supersaturation also starts to diminish. Both of these factors could account for the decreasing hardness. The presence of a high fraction of high diffusivity grain boundary paths would greatly speed up the process of loss of supersaturation. The fact that loss of hardness occurs much sooner at higher temperatures could suggest it is mainly due to diffusion of transition elements, e.g. Cr, Mo, and W, which are substitutional atoms, and is not principally a result of loss of supersaturation of interstitial B and C which are mobile even at low temperatures.

5. Conclusions

(i) Gas-atomised Fe–18.9 at.%Cr–16.1 at.%B–4.0 at.%C–2.8 at.%Si–2.4 at.%Mo–1.9 at.%Mn–1.7 at.%W powder ($Fe_{52}Cr_{19}Si_3Mo_2W_2Mn_2B_{16}C_4$) contains a mixture of amorphous and crystalline powder particles with crystalline phases α-Fe and $Fe_{1.1}Cr_{0.9}B_{0.9}$. The microstructure of the HVOF-sprayed coatings is composed of splat-like regions arising from rapid solidification of fully molten powder and near-spherical/deformed spherical regions which come from

partially melted powder and having a microstructure retained from the original powder feedstock material.

(ii) DSC analysis of powder and coating samples reveals that in both of these devitrification proceeds by a two stage process with pronounced crystallization peaks at approximately 640 and 840 °C for the powder and 640 and 780 °C for the coating. The powder is estimated to contain ~18 wt.% of amorphous phase whereas there is calculated to be around 50% of amorphous phase in the coating. This is attributed to the higher cooling rate of splats compared with gas-atomised powders.

(iii) In annealing experiments at 550, 650, 750 and 925 °C for 60 min, it is found that the first evidence for crystallization is at 650 °C but only α-Fe and $Fe_{1.1}Cr_{0.9}B_{0.9}$ are found. At 750 and 925 °C, there is clear evidence for the formation of $M_{23}C_6$ as well as α-Fe and $Fe_{1.1}Cr_{0.9}B_{0.9}$. The devitrification behaviour of powder and coatings follow broadly similar patterns.

(iv) The hardness of the coatings can be increased by annealing above 550 °C but the increase depends on the temperature and time of heat treatment. For a fixed time of 60 min, the as-sprayed hardness of 9.2 GPa is increased significantly at 650 °C and 750 °C but little changed at 925 °C. By annealing for various times at 650 and 750 °C, the peak hardnesses were found to be 12.5 and 11.8 GPa, respectively. With longer annealing times hardness decreased rapidly from the peak value.

Acknowledgements

K. Chokethawai acknowledges financial support from the Royal Thai Government Science and Technology, under contract No. 08/2544 for a PhD studentship at the Department of Mechanical, Materials and Manufacturing Engineering, Faculty of Engineering, University of Nottingham, Nottingham, UK.

References

[1] L. Pawlowski, The Science and Engineering of Thermal Spray Coatings, Wiley, Chichester, UK, 1995.
[2] H. Voggenreiter, H. Huber, S. Beyer, H.-J. Spies, in: C.C. Berndt, S. Sampath (Eds.), Proceedings of the 8th National Thermal Spray Conference—Advances in Thermal Spray Science and Technology, September, 1995, Houston, TX, USA, ASM International, Materials Park, OH, USA, 1995, pp. 303–308.
[3] H.L. de Villiers Lovelock, J. Therm. Spray Technol. 7 (1998) 357–373.
[4] K.O. Legg, M. Graham, P. Chang, F. Rastagar, A. Ganzales, B. Sartwell, Surf. Coat. Technol. 81 (1996) 99–105.
[5] W.L. Johnson, ASM Metals Handbook, vol. 2, 10th edition, ASM International, Metal Park, OH, USA, 1990, p. 804.
[6] S.K. Das, E.M. Norin, R.L. Bye, in: B.H. Kear, B.C. Giessen (Eds.), Rapidly Solidified Metastable Materials, Mater. Res. Soc. Symp. Proc., vol. 28, Materials Research Society, Pittsburgh, PA, USA, 1984, pp. 233–237.
[7] A.H. Dent, A.J. Horlock, D.G. McCartney, S.J. Harris, Mater. Sci. Eng. A 283 (2000) 242–250.
[8] H.W. Jin, Y.M. Rhyim, S.G. Hong, C.G. Park, Mater. Sci. Eng. A 304–306 (2001) 1069–1079.
[9] K. Kishitake, H. Era, F. Otsubo, J. Therm. Spray Technol. 5 (2) (1996) 145–153.
[10] A. Inoue, Bulk Amorphous Alloys, Trans Tech Publications, Zurich, 1998.
[11] S.J. Pang, T. Zheng, K. Asami, A. Inoue, Acta Mater. 50 (2002) 489–497.
[12] D.J. Branagan, W.D. Swank, D.C. Haggard, J.R. Fincke, Metall. Mater. Trans. A 32 (10) (2001) 2615–2621.
[13] A.P. Wang, T. Zhang, J.Q. Wang, Mater. Trans. 46 (2005) 1010–1015.
[14] A.P. Wang, T. Zhang, J.Q. Wang, Philos. Mag. Lett. 86 (2006) 5–11.
[15] D.J. Branagan, M. Breitsameter, B.E. Meacham, V. Belashchenko, J. Therm. Spray Technol. 14 (2005) 196–204.
[16] D.J. Branagan, Y. Tang, Composites A 33 (2002) 855–859.
[17] Y. Wu, Mater. Sci. Eng. A 430 (2006) 34–39.
[18] D. Zhang, D.G. McCartney, S.J. Harris, Mater. Sci. Eng. A 344 (2003) 45–56.
[19] H.E. Kissinger, Anal. Chem. 29 (1957) 32.
[20] K. Lu, Mater. Sci. Eng. R 16 (1996) 161–221.
[21] S. Kamnis, S. Gu, N. Zeoli, Surf. Coat. Technol. 202 (12) (2008) 2715–2724.
[22] C. Moreau, P. Cielo, M. Lamontagne, S. Dallaire, J.C. Krapez, M. Vardelle, Surf. Coat. Technol. 46 (1991) 173–187.
[23] A.J. Yule, J.J. Dunkley, Atomization of Melts: For Powder Production and Spray Deposition (Oxford Series on Advanced Manufacturing), Oxford University Press, Oxford, UK, 1994.
[24] T. Koziel, A. Zielinska-Lipiec, Z. Kedzierski, T. Czeppe, J. Microsc. 224 (1) (2006) 27–29.
[25] T.A. Baser, M. Baricco, J. Alloys Compd. 434–435 (2007) 176–179.
[26] Q.J. Chen, H.B. Fan, J. Shen, J.F. Sun, Z.P. Lu, J. Alloys Compd. 407 (2006) 125–128.
[27] J.W. Graydon, S.J. Thorpe, D.W. Kirk, Acta Metall. Mater. 43 (1995) 1363–1373.
[28] Z.C. Zhong, X.J. Jiang, A.L. Greer, Mater. Sci. Eng. A 226–228 (1997) 531–535.